Role of the chemical homogenization on the microstructural and mechanical evolution of prolonged heat-treated laser powder bed fused Inconel 625

Role of the chemical homogenization on the microstructural and mechanical evolution of prolonged heat-treated laser powder bed fused Inconel 625

Giulio Marchese*, Emilio Bassini, Simone Parizia, Diego Manfredi, Daniele Ugues, Mariangela Lombardi, Paolo Fino, Sara Biamino

Department of Applied Science and Technology, Politecnico di Torino, Corso Duca degli Abruzzi 24, 10129 Torino, Italy.

***** *Correspondence: giulio.marchese@polito.it; Tel.: +39-011-090-4763*

Abstract

Ni-based superalloy components for high-temperature applications rely on the long term stability of the microstructure and mechanical properties at service temperatures. Nowadays, the production of such types of components is frequently performed via Additive Manufacturing (AM) technologies. Nevertheless, few studies are dedicated to understanding the behavior of AM Ni-based superalloys upon prolonged exposure to high temperatures. This work aims at studying the effect of prolonged thermal exposures on the microstructure and mechanical properties of Inconel 625 processed by laser powder bed fusion. Thermal exposures within the range of 600 °C and 900 °C for 200 hours were performed on this material. The as-built and solution annealed Inconel 625 conditions were selected. The solution annealed state implies a complete chemical homogenization, typically recommended for working at high temperatures, whereas the initial as-built state is characterized by segregations and fine dendritic structures. Upon the studied prolonged thermal exposures, the peculiar as-built microstructure formed a higher quantity of phases with smaller dimensions with respect to the solution annealed condition under thermal exposures. The smaller phases of the as-built state resulted in similar mechanical properties evolution under different temperatures. Differently, the prolonged heat-treated solution annealed conditions exhibited more marked mechanical properties variations due to coarser phases.

Keywords: Laser powder bed fusion; Inconel 625; Ni-based superalloys, mechanical properties, δ phases.

1.0 Introduction

Laser powder bed fusion (LPBF) is an additive manufacturing process nowadays widely applied for the production of different metallic complex parts due to its exceptional net-shape manufacturing capability [1–4]. This technology can be especially attractive for processing Ni-based superalloys having limited machinability [5,6].

Among the processed LPBF Ni-based superalloys, materials with high weldability, such as Inconel 718 and Inconel 625 (IN625), typically exhibit low residual porosities, whereas materials with low weldability such as CM247LC and Inconel 738 tend to suffer from cracks formation [7–10]. Moreover, even Hastelloy X alloy characterized by good weldability could suffer from crack susceptibility when processed by LPBF process [11–14].

Considering the current LPBF Ni-based superalloys, IN625 alloy presents good mechanical properties at high temperatures, correlated to remarkable high oxidation and corrosion resistance in harsh conditions (up to around 980 °C) [15,16].

Upon high temperatures exposure, the alloy is subjected to phases formation accompanied by mechanical properties modifications. Several studies on the effect of different prolonged thermal exposures on the microstructure and mechanical properties of traditional heat-treated IN625 alloy were reported [17–22]. In these works, the evolution of the phases is demonstrated to be the critical factor governing the mechanical properties of the alloy. The formation of metastable γ" phases (Ni_3Nb – body-centered tetragonal) results in the mechanical enhancement of the alloy around 550 °C – 750 °C, whereas the formation of its stable form, δ phases (Ni_3Nb – orthorhombic), is detrimental for ductility and toughness. Especially, prolonged thermal exposures within 650 °C - 900 °C lead to the marked formation of δ phases, reducing the material ductility. Moreover, embrittling intermetallic Laves phases (hexagonal structures – $(Cr,Fe,Ni)_2(Si,Ti,Nb,Mo)$) and different types of carbides (MC, M_6C, and $M_{23}C_6$ types) under thermal exposures can be formed [18,22,23].

However, the microstructure of LPBF IN625 is extremely different with respect to the traditional wrought IN625, influencing its properties as well as its microstructure evolution under thermal exposures. Nowadays, the primary studies have been focused on the microstructure and properties of the LPBF IN625 in as-built and heat-treated conditions.

For instance, the LPBF IN625 is characterized by higher corrosion resistance than wrought IN625 state [24,25]. This can be attributed to the presence of sub-micrometric dendritic/cellular structures with interdendritic segregations (mainly Nb and Mo) [26–29]. These microstructural features derive from the rapid solidification (cooling rates around 10^5-10^6 °C/s [9,30]).

Different studies highlighted the role of segregations in LPBF IN625 on phases formation for short thermal exposures. As for the stress relieved LPBF IN625, it was demonstrated that the typical temperature (870 °C) induces the fast kinetic of δ phases formation with respect to the heat-treated

wrought IN625 alloy, due to the interdendritic segregations [31–33]. In order to reduce the high residual stresses and to limit the concentration of the embrittlement δ phases, an alternative stress relieving treatment at 800 °C was also investigated [31,32]. In particular, Lass et al. [33] studied the effect of the typical stress relieving temperature (870 °C) for different soaking times. Through transmission electron microscopy analysis, the authors of this study pointed out that thermal exposures for 8 hours could form γ" phases along with δ phases at interdendritic regions. Based on the traditional literature on IN625 alloy, a similar thermal exposure should not generate γ" phases [16,18].

Recrystallization annealing and solution annealing treatments can be performed to homogenize the material dissolving the segregations, as well as to induce grain modifications. The studies revealed that, upon such heat treatments, recrystallization occurs with the formation of equiaxed grains with small carbides (e.g., MC or M_6C carbides) [26,27,34–36]. Kreitcberg et al. [34] investigated the formed phases of LPBF IN625 subjected to different heat treatments, including recrystallization annealing and solution annealing treatments, correlating the resulting microstructure with the tensile properties. The dimensions and type of the phases strongly depend on the chemical composition of the starting powder, as well as on the temperature, time, and cooling rates employed.

Considering that IN625 is typically employed at high temperatures, it is crucial to investigate its microstructure under prolonged thermal exposures. Nevertheless, only recently, the research has been paid attention to the study of microstructure and mechanical properties evolution of LPBF IN625 alloy under prolonged thermal exposures. For instance, Inaekyan et al. [36] reported the tensile properties of post heat-treated LPBF IN625 upon thermal exposures at 760 °C and 980 °C for 100 hours assessed against the original states.

Therefore, particular emphasis should be given on investigating microstructure, and mechanical properties of post heat-treated LPBF IN625 alloy, simulating the operative temperature of the components. Moreover, the microstructure evolution induced by different levels of chemical homogenization should also be considered.

For these reasons, in this work, to study the effect of the prolonged thermal exposures on LPBF IN625, two conditions with different levels of chemical homogenization were selected and compared. The as-built condition, which is characterized by segregations and the solution annealed state with homogenous chemical composition. The results pointed out the different microstructure and tensile properties development.

2.0 Material and methods

2.1 Starting IN625 powder

Gas atomized IN625 powder supplied by EOS GmbH was employed. The chemical composition of the used powder was analyzed by scanning electron microscope (SEM, Phenom XL) equipped with an energy dispersive spectroscopy (EDS) detector. The C was determined by means of combustion infrared analysis (using LECO – analyzer). The evaluated chemical composition (Table 1) resulted in being under the chemical composition described in the UNS N06625.

Table 1 –Chemical composition (in wt %) obtained by EDS analysis and combustion infrared analysis (for carbon).

Ni	Cr	Mo	Fe	Nb	Co	Si	Ti	Al	C
66.1	19.3	8.6	0.6	4.1	0.1	0.4	0.4	0.4	0.012

The particles mainly exhibited quite spherical shapes with the presence of satellites, as displayed in Figure 1. The particle size distribution was characterized by a d10 of 16 μm, d50 of 27 μm and d90 of 48 μm obtained using laser granulometry diffraction with a Fritsch Analysette 22 Compact model.

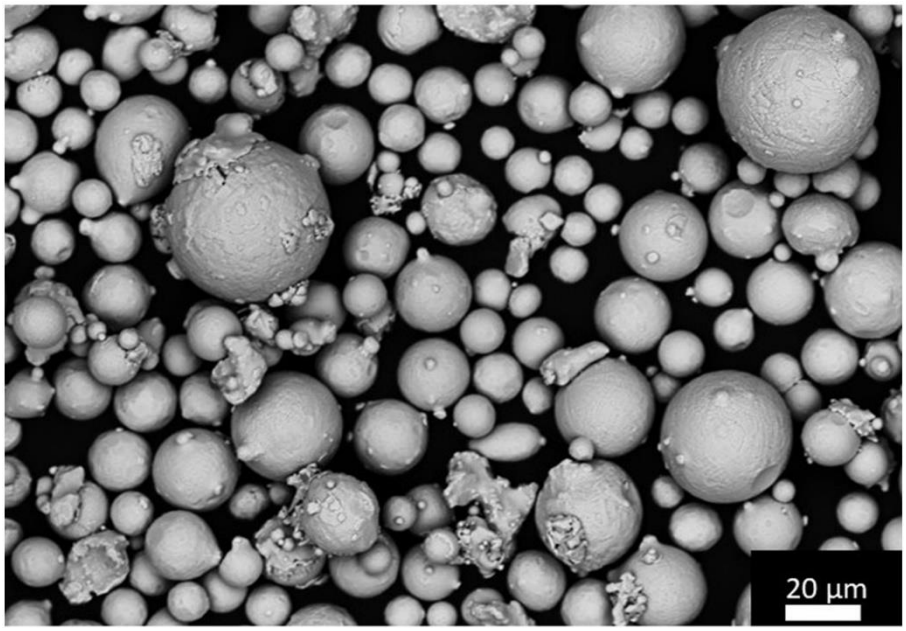

Figure 1 - SEM image of particles of IN625 alloy

2.2 Samples characterization

Cubic samples with dimensions of 15 x 15 x 15 mm^3 and cylindrical specimens with a length of 110 mm and a diameter of 15 mm were built along the building direction. The samples were fabricated using an EOS M270 Dual mode version under argon atmosphere with the building platform kept at 80 °C, applying specific process parameters aiming at minimizing the residual porosity. A laser power of 195 W, scanning speed of 1200 mm/s, hatching distance of 0.09 mm, and layer thickness of 0.02 mm, using the EOS laser scanning rotation of 67° were applied. These operating process parameters were employed in previous studies [26,35].

A part of the cubic samples and cylinders were solution annealed at 1150 °C for 2 hours, followed by water quenching, as typically recommended for this alloy [37,38]. Subsequently, the as-built samples and the solution annealed samples (abbreviated hereafter as AB and SOL, respectively) were subjected to thermal exposures from 600 to 900 °C for 200 hours. All the heat treatments were carried out in a muffle furnace, followed by water quenching to freeze the high-temperature microstructure. The investigated thermal exposures are reported in Figure 2.

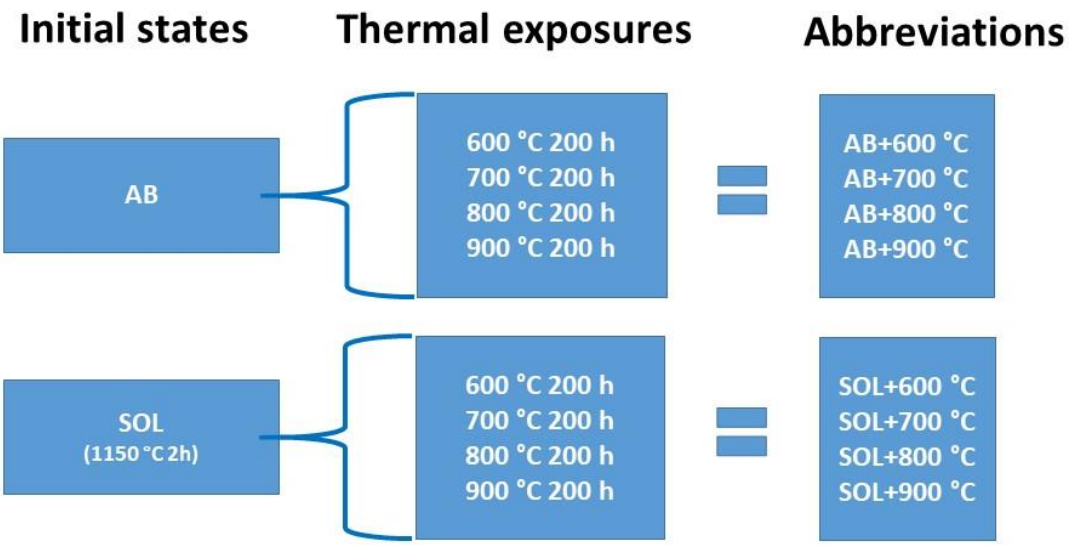

Figure 2 – Schematic diagram of the investigated prolonged heat-treated conditions performed on the initial AB and SOL states.

The samples were cut along the building direction, then ground by means of silicon carbides (SiC) papers, and finally polished down to 1 µm using diamond suspensions. This orientation was chosen to observe the columnar grains of the AB conditions. Differently, the SOL states present equiaxed grains both along the building direction and perpendicular to the building direction. For microstructural observations, the samples were etched with Kalling's No.2 reagent. The microstructure was analyzed by

a light optical microscope (LOM - Leica DMI 5000 M), a scanning electron microscope (SEM, Phenom XL), and a field emission scanning electron microscope (FESEM - Zeiss SupraTM40) equipped with energy dispersive spectroscopy (EDS) detector. The formation of phases was examined by X-ray diffraction (XRD, PANalytical) with Cu K_α radiation at 40 kV and 40 mA in a Bragg Brentano configuration operating with a step size 0.013 and 25 s per step.

It should be noted that the formed phases for the samples subjected to thermal exposures at 600 °C and 700 °C were determined by the time-temperature-transformation (TTT) diagram of the alloy coupled to the typical morphology of the phases reported in the literature. More in detail, for IN625 alloy, this temperature range promotes mainly the formation of γ" phases (with spherical or elliptical shapes) and δ phases (with acicular forms) [16,18,22,23,39]. On the other hand, for the prolonged thermal heat-treated samples at 800 °C and 900 °C, the identification of the phases was also supported by FESEM+EDS and XRD analyses due to superior sizes and large phases concentration.

Finally, tensile tests were performed using a Zwick-Roell BT1 - FR100 at room temperature, applying a strain rate of $8.10^{-3}s^{-1}$. For the tensile tests, cylindrical samples were machined to prepare tensile specimens under the ASTM E8/E8M-09. For each condition, in order to provide an average value and standard deviation, three tensile specimens were employed. The samples were built along the building direction.

3.0 Results and discussion

3.1 AB and SOL conditions overview

The microstructure of LPBF IN625 samples consisted of a network of very fine dendritic architectures with columnar and cellular shapes distributed throughout all the melt pools, as displayed in Figure 3a. Typically, these structures reach dimensions approximately up to 1 μm [26,29,30]. The largest dendrites are mainly close to the melt pool contours. This peculiar microstructure derived from the rapid solidification of the LPBF process (around 10^6 °C/s [9]).

During solidification, the dendritic regions solidify faster than the interdendritic areas, and these last areas tend to be highly enriched in segregating elements, being mainly Nb and Mo, in the case of IN625. A similar microstructure can strongly affect the formation of the phases, especially those containing Nb. This chemical element plays a primary role in the formation of the main precipitates, the metastable strengthening γ" phase, as well as its stable form, the embrittled δ phase.

On the contrary, the SOL treatment dissolves the dendritic structures and the melt pools, homogenizing the chemical composition as well as involving recrystallization and grain growth, leading

to the formation of equiaxed grains (Figure 3b). Additionally, the SOL microstructure reveals the presence of sub-micrometric carbides that decorate the material. A detailed description of the AB and SOL states is provided in a previous investigation [26].

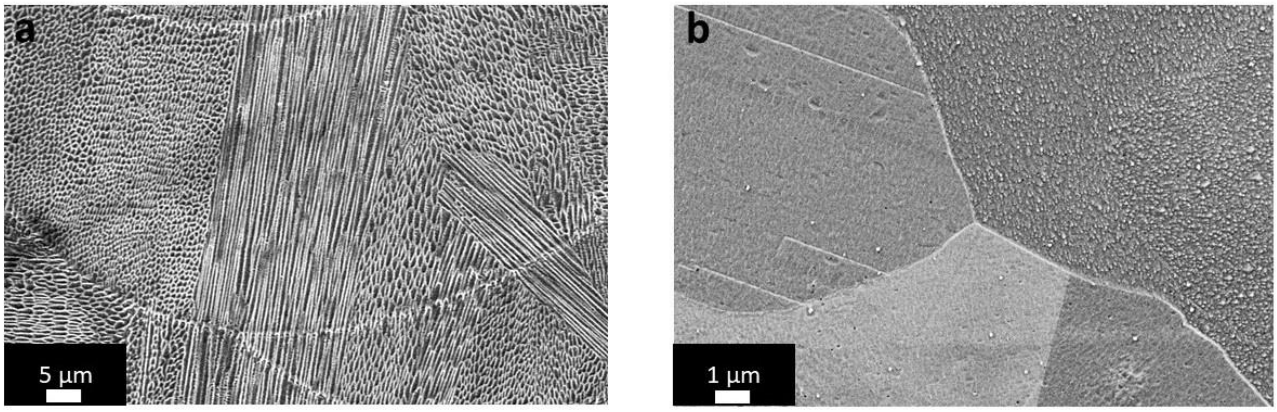

Figure 3 – (a) SEM image of AB state showing the very fine dendritic architectures; (b) FESEM image of SOL state exhibiting sub-micrometric carbides. Kalling's No.2 reagent was used.

3.2 Microstructure evolution under prolonged thermal exposures

Figure 4 shows the microstructure evolution of AB and SOL states upon thermal exposure ranging from 600 to 900 °C for 200 hours.

The AB material revealed columnar grains extended through several melt pools along the building orientation (z-axis). After thermal exposures at 600 °C, the microstructure was very similar to the AB state, without exhibiting any precipitation of phases that could be detected by LOM analysis. On the other hand, phases started decorating the grain boundaries after thermal exposures at 700 °C, 800 °C, and 900 °C. However, no large intragranular phases were detected even at these temperatures. Moreover, within the studied prolonged thermal exposures, it is worth underlining that recrystallization phenomena did not occur and that the melt pool dissolution occurred only for temperatures exceeding 700 °C.

Equiaxed grains with annealing twin boundaries constitute the SOL microstructure along z-orientation. After thermal exposures at 600 °C, precipitates gradually tended to decorate the grain boundaries. During the investigation, it was observed that the average size of grains remained constant under the prolonged thermal exposures, probably due to the presence of intergranular precipitates hindering their growth. Additionally, remarkable intragranular coarse precipitation occurred for thermal exposures at 800 °C and 900 °C. It is worthwhile to note that the SOL+900 °C exhibited the presence of elongated precipitates (also reaching length around 50 µm), almost crossing the grains, giving the illusion of the formation of small grains.

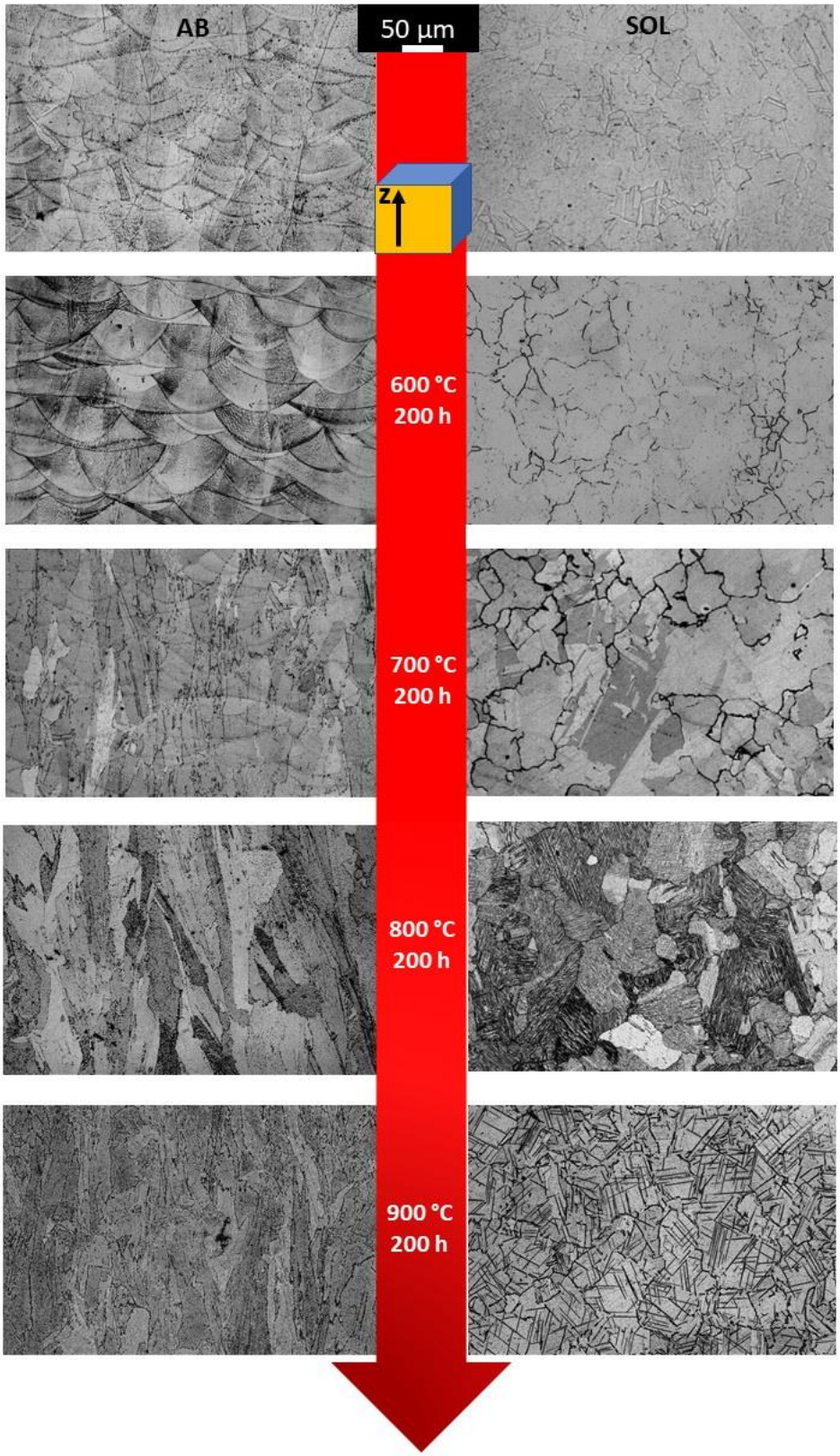

Figure 4 – LOM images of prolonged heat-treated LPBF IN625 material: AB and SOL conditions heat-treated at 600°C, 700 °C, 800 °C and 900 °C for 200 hours. Kalling's No.2 reagent was used.

Figure 5 displays the microstructure evolution of the AB and SOL conditions heat-treated at 600 and 700 °C for 200 hours. Intense precipitation of γ" phases is evident. The AB+600 °C state (Fig. 5a and b) revealed γ" phases of about 200 nm close to grain boundaries and within interdendritic areas. Moreover, nanometric γ" phases at the dendritic core that are regions depleted in Nb could be detected. The SOL+600 °C state (Fig 5c and d) exhibited nanometric γ" phases dispersed throughout the material with the larger ones located along the grain boundaries and reaching a length of around 600 nm.

As for the AB+700 °C state (Fig 5e and f), intergranular and interdendritic δ phases together with homogeneously dispersed nanometric γ" phases were detected. As far as the SOL+700 °C state (Fig 5g and h) is concerned, the formation of intergranular δ phases mainly occurred. However, isolated intragranular δ phases were also reported. Furthermore, high magnification images (Fig. 5h) highlighted the formation of fine γ" phases.

Comparing the dimensions of the phases detected in AB and SOL states upon prolonged thermal exposures, it is interesting to note that the SOL+600 °C state revealed larger intergranular γ" phases than the AB+600 °C one, and that the SOL+700 °C state revealed coarser δ phases than the AB+700 °C one. This can be ascribed to the homogenous availability of Nb within the matrix in the solution annealed state. On the contrary, the AB state is characterized by a high amount of Nb entrapped in the interdendritic areas, thus limiting the amount of Nb available for the phases formation.

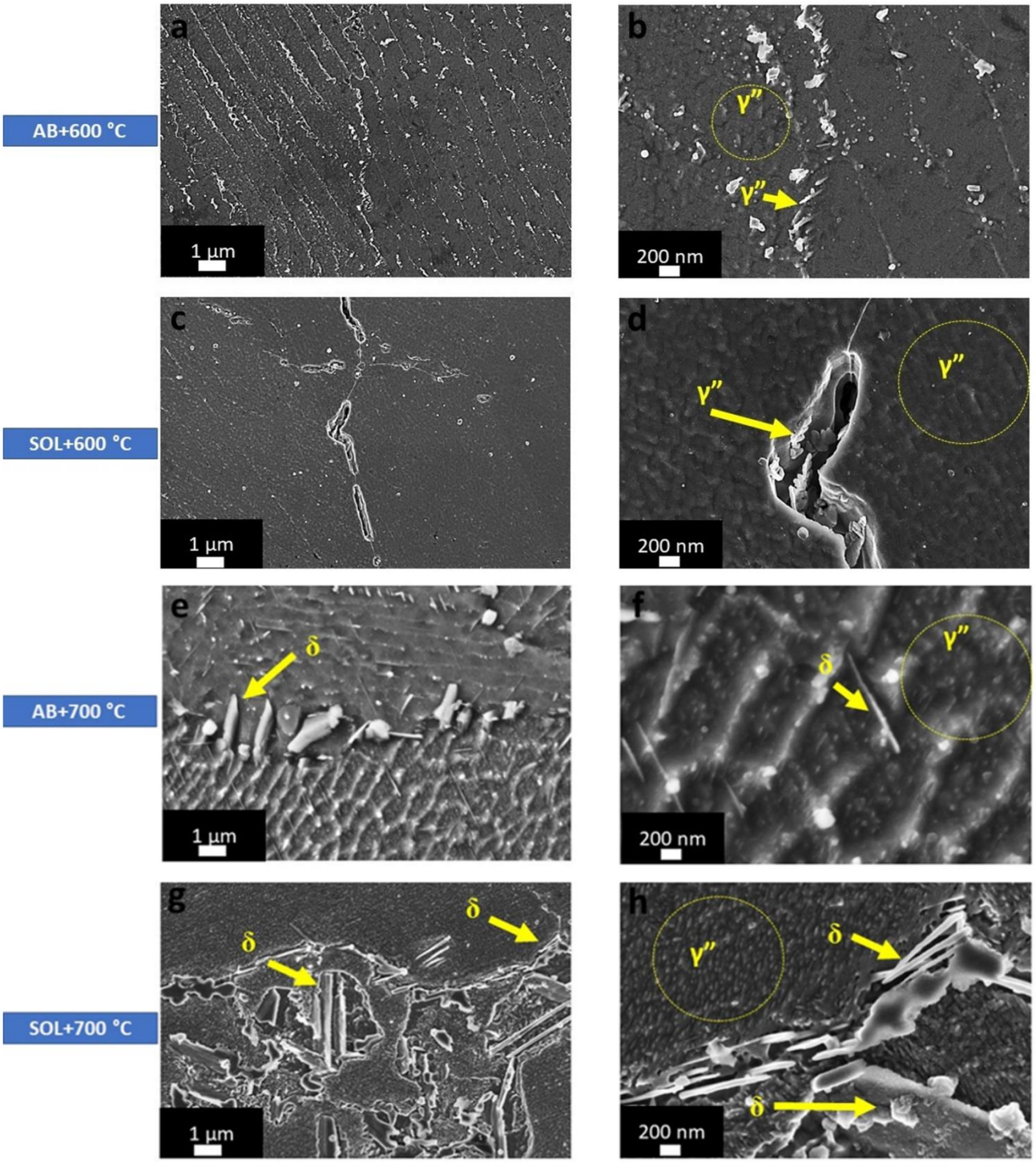

Figure 5 - SEM and FESEM images of prolonged heat-treated AB and SOL for 200 hours: (a and b) AB+600 °C, (c and d) SOL+600 °C, (e and f) AB+700 °C, (g and h) SOL+700 °C. The samples revealed the presence of γ” phases as indicated by yellow circles and yellow arrows as well as δ phases highlighted by yellow arrows. Kalling’s No.2 reagent was used.

Figure 6 shows the microstructure evolution of the AB and SOL conditions thermally exposed at 800 and 900 °C for 200 hours, with δ phases pointed out in the images. The thermal exposures at 800 °C and 900 °C drastically modified the microstructure of the two initial states. For the AB states (Fig. 6a, b, e, and f), the microstructure revealed the formation of inter/intragranular δ phases throughout the material. The prolonged thermal exposure on SOL states (Fig. 6c, d, g, and h) produced the formation of the largest detected δ phases within the grains. Comparing the microstructures of the samples exposed to these high test temperatures with those exposed to lower temperatures, it is evident that the kinetics of nucleation and growth of the δ phase change with temperature. The SOL+800 °C (Fig. 6c and d) exhibited a larger number of δ phases nuclei, coupled to their slower growth rate, with respect to the SOL+900 °C (Fig. 6g and h).

Comparing the AB and SOL microstructure evolution under thermal exposure, the SOL state presented the homogenous distribution of Nb within the alloy allowing the growth of δ phases throughout the whole material. On the contrary, for the AB state, the formation of δ phases occurred in the interdendritic and grain boundaries areas enriched in Nb.

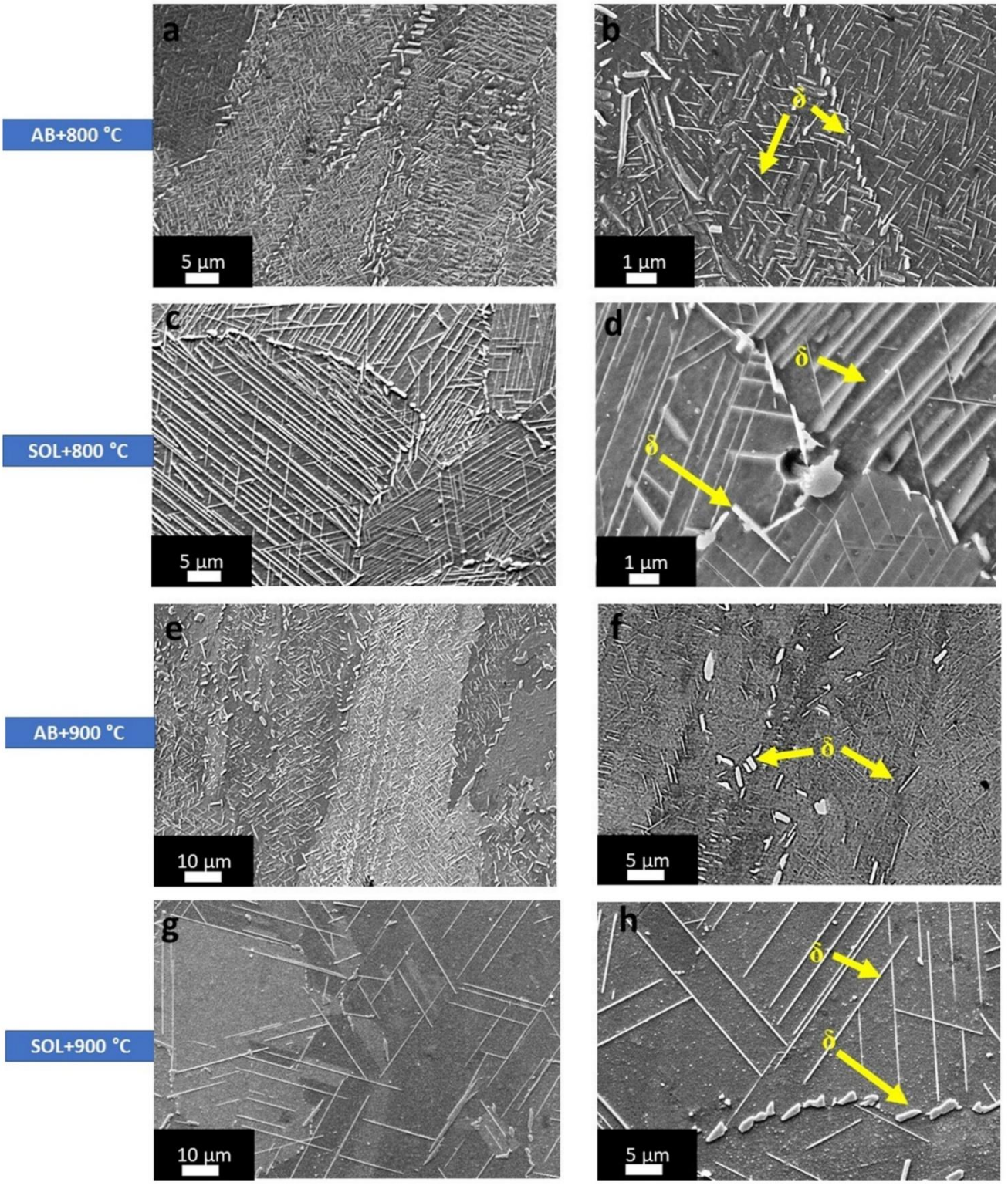

Figure 6 - SEM and FESEM images of prolonged heat-treated AB and SOL samples for 200 hours: (a and b) AB+800 °C, (c and d) SOL+800 °C, (e and f) AB+900 °C and (g and h) SOL+900 °C. The samples revealed the presence of δ phases as indicated by yellow arrows. Kalling's No.2 reagent was used.

3.3 Phases detection

Based on the TTT diagram of the alloy and the morphology of the precipitates observed in the SEM/FESEM investigation, the majority of the formed phases can be ascribed to γ" phases for thermal exposures at 600 °C and γ" phases and δ phases for thermal exposures at 700 °C [16,18,22,23,39]. Only a very low quantity of carbides could be formed considering the very low level of C in the starting powder (Table 1). Moreover, a minor formation of Laves phases could occur.

For all the conditions, the XRD patterns (Fig. 7) revealed the peaks of the austenitic matrix (γ matrix). Additionally, it was possible to detect the peaks of δ phases for the AB+800 °C, AB+900 °C, SOL+800 °C, and SOL+900 °C samples. On the contrary, for samples thermally exposed at a temperature of 700 °C, the δ phases concentration was below the detection threshold of the instrument.

For thermal exposed LPBF IN625, the XRD peaks of δ phases (012) and (211) were also detected in the literature [31,33].

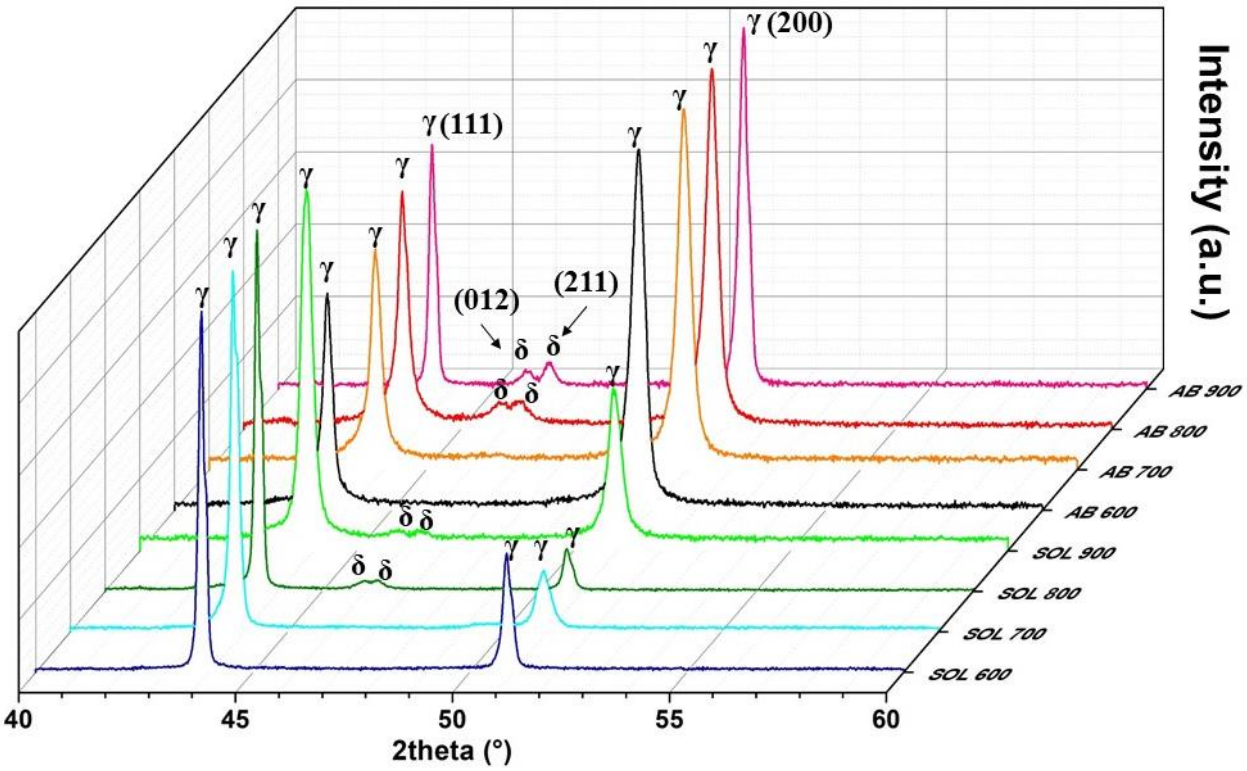

Figure 7 –XRD patterns of the prolonged thermal exposure conditions from 600 to 900 °C along the building direction (z-axis).

From the intensity of the peaks of the δ phases (Fig. 8) of the AB+800 °C, SOL+800 °C, AB+900 °C, and SOL+900 °C, it is possible to estimate the quantity of the δ phases. The results revealed a higher intensity for the prolonged heat-treated AB states than for the prolonged heat-treated SOL ones. This indicates a larger fraction of phases for the prolonged AB states, that can be ascribed to a large number of sites for the initial phases nucleation, which are constituted by the interdendritic areas and grain boundaries. The precipitates growth is limited by the presence of areas depleted of Nb, due to its inhomogeneous distribution in the AB samples, as observed by the SEM/FESEM analyses. On the other hand, the prolonged thermal exposed SOL states, present a lower amount of this phase, which tends to grow more rapidly, achieving larger final dimensions than the AB state. The reason for such behavior lies in the very homogeneous chemical composition throughout the whole matrix.

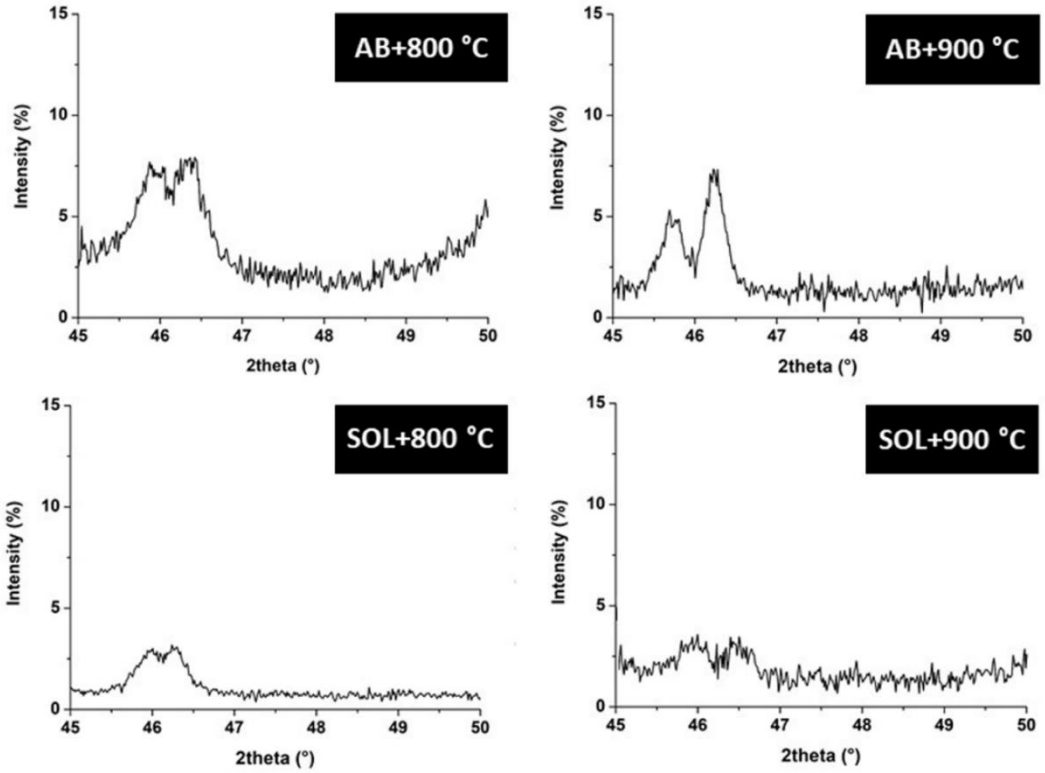

Figure 8 - zoom of XRD patterns of the peaks of δ phases for the AB+800 °C, AB+900 °C, SOL+800 °C, and SOL+900 °C.

The formation of δ phases was also supported by the EDS analysis performed on the prolonged heat-treated conditions at 800 °C and 900 °C displayed in Figure 9. The EDS scan lines revealed that the acicular phases were enriched in Nb with an almost constant level of Ni compared to the matrix, thus indicating a high concentration of Nb and Ni within the phases. These are the main forming chemical elements of δ phase, which highlighted its formation.

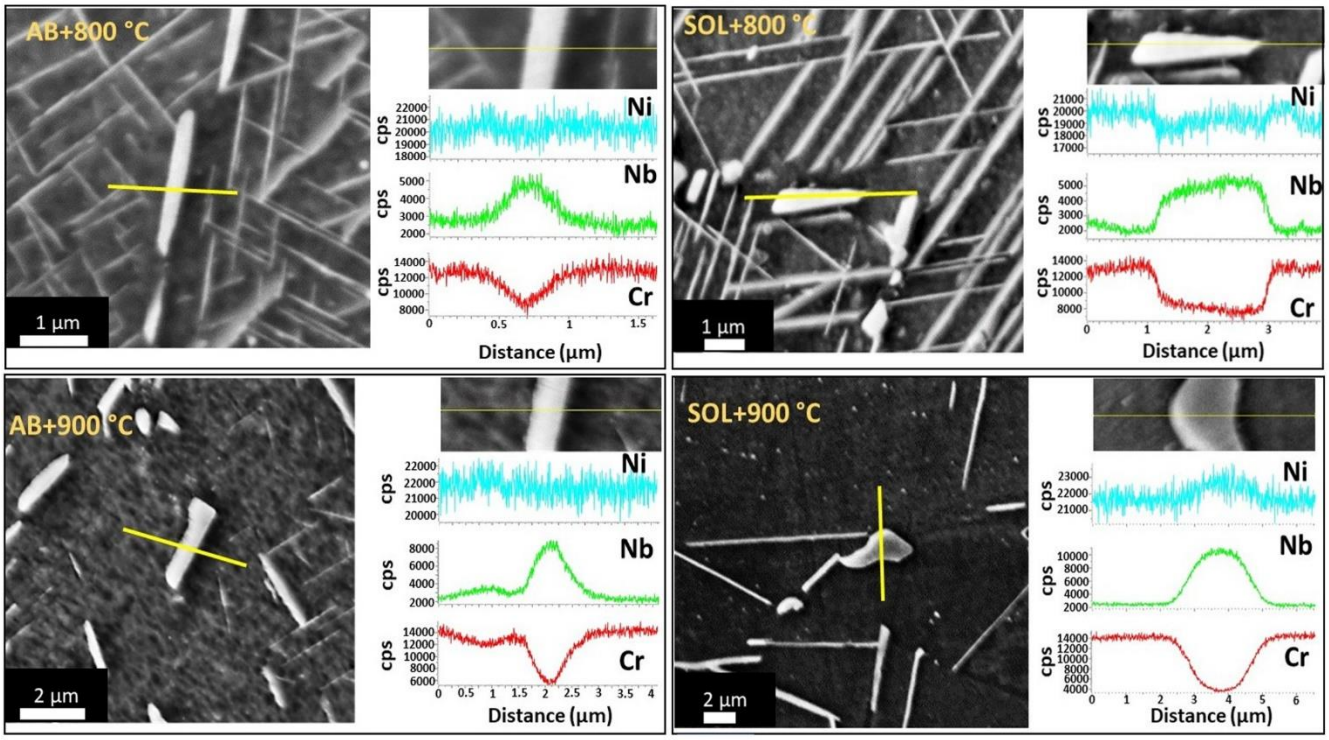

Figure 9 - EDS scan lines performed on the prolonged heat-treated states; counts per seconds (cps).

3.4 Tensile properties

The tensile properties of the initial AB and SOL conditions and prolonged thermal exposed conditions are provided in Figure 10 and Table 2.

The prolonged heat-treated conditions revealed an increment of the tensile strengths (yield and ultimate tensile strengths) coupled to a decrement of the elongations at failure with respect to the AB and SOL state, respectively. The trend of the mechanical properties resulted to be different caused by the different microstructure evolution of AB and SOL states.

For the AB states, the AB+600 °C and the AB+700 °C conditions the increment of tensile strength can be attributed to the formation of γ" phases, which is the main strengthening phase for IN625 alloy [18,40]. Even if the AB+800 °C did not show γ" phases, the tensile properties result to be similar to the AB+700 °C due to the high amount of δ phases (as indicated by XRD analysis in Fig. 7). The AB+900 °C state reports an inferior increment of tensile strengths compared to the other prolonged heat-treated AB conditions. The δ phases formation indeed tends to increase the tensile strength, but the high thermal exposure (900 °C) dissolved the interdendritic structures, reducing the tensile strength. The presence of phases formation provoked a reduction of the ductility, while the dendritic dissolution of the AB+900 °C

conditions limited the ductility degradation with respect to AB+600 °C, AB+700 °C and AB+800 °C conditions.

For the SOL conditions, after thermal exposures at 600 °C and 700 °C occur the generation of γ" phases. The maximum tensile strengths were achieved at 700 °C derived from the high precipitations of γ" phases. The SOL+800 °C and the SOL+900 °C states present lower mechanical strengths than the SOL+600 °C and the SOL+700 °C conditions. This can be correlated to the large dimensions of δ phases within the samples. For the SOL+800 °C and the SOL+900 °C, the large sizes of the δ phases conditions are displayed in the FESEM images (Fig. 6).

It is interesting to note that the presence of segregations of the AB state, tends to involve similar mechanical properties for a temperature range of 600 - 800 °C. On the other hand, the SOL state presents homogenous chemical distribution giving the possibility to generate larger phases, and therefore, involving greater mechanical properties modifications under the same temperature range.

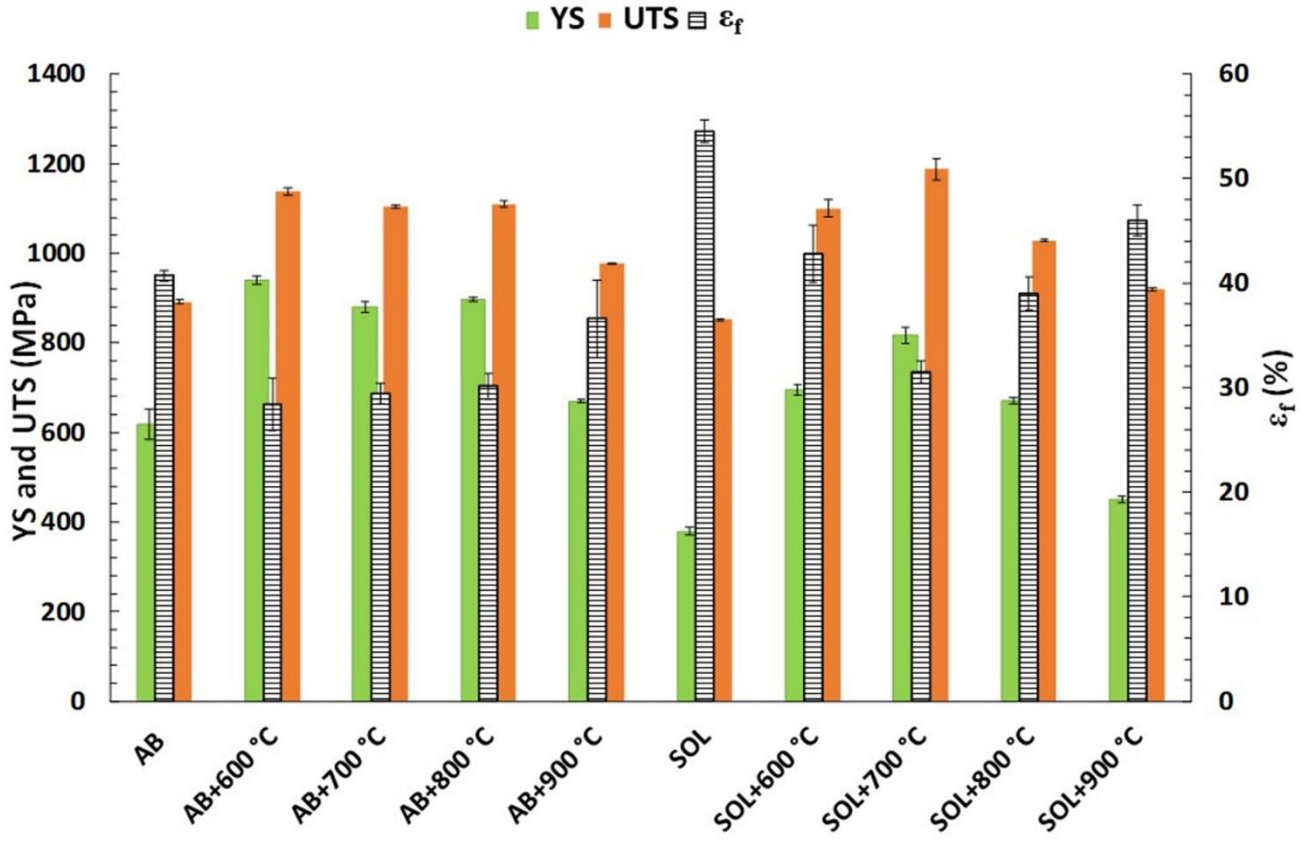

Figure 10 – Tensile properties of AB, SOL, and prolonged heat-treated conditions. The tensile properties are abbreviated as yield strength (YS), ultimate tensile strength (UTS) and elongation at failure (ε_f).

Table 2 – Average value and standard deviation of the tensile properties of the AB, SOL, and prolonged thermal exposure conditions; samples were built along the building direction (z-axis). The tensile properties are reported as yield strength (YS), ultimate tensile strength (UTS) and elongation at failure (ε_f).

LPBF IN625 Condition	YS (MPa)	UTS (MPa)	ε_f (%)
AB [35]	618 ± 33	891 ± 5	40.7 ± 0.5
AB+600 °C	940 ± 9	1137 ± 8	28.4 ± 2.5
AB+700 °C	879 ± 12	1104 ± 4	29.4 ± 1.0
AB+800 °C	896 ± 5	1110 ± 7	30.1 ± 1.2
AB+900 °C	669 ± 4	977 ± 2	36.6 ± 3.7
SOL [35]	379 ± 9	851 ± 3	54.5 ± 1.1
SOL+600 °C	694 ± 12	1100 ± 19	42.8 ± 2.7
SOL+700 °C	817 ± 18	1187 ± 25	31.5 ± 1.1
SOL+800 °C	670 ± 7	1028 ± 2	39.0 ± 1.6
SOL+900 °C	450 ± 8	920 ± 4	46.0 ± 1.5

3.5 Fracture surfaces

The fracture surfaces of the initial (AB and SOL) and prolonged heat-treated conditions are reported in Figure 11. The brittle fractures that may arise from the intergranular phases are indicated by red arrows, while the small dimples associated with ductile fractures are highlighted by yellow dash arrows. Under thermal exposures, the AB and SOL samples revealed the increment of brittle fractures due to the formation of the phases. It is well known the embrittling influence of δ phases as well as a high concentration of γ" phases [41]

For AB+600 °C, the cracks were involved by the presence of interdendritic and intergranular γ" phases. For the AB+700 °C derived from both γ" and δ phases. For AB+800 °C and AB+900 °C states, the intergranular δ phases could be the main crack initiators. The SOL samples exhibited extended ductile features with a lower amount of brittle portions with respect to the AB samples. Under prolonged thermal exposures at 600 °C, the fracture surface did not show marked alterations due to the fine size of the intergranular γ" phases. However, the SOL+700 °C revealed a very large quantity of brittle fractures and number of secondary cracks due to δ phases and high concentration of γ" phases. This is also evident by the marked ductility degradations with respect to the other prolonged thermal exposed SOL states. For the SOL+800 °C and SOL+900 °C, the fracture exhibits some brittle areas associated with large δ phases.

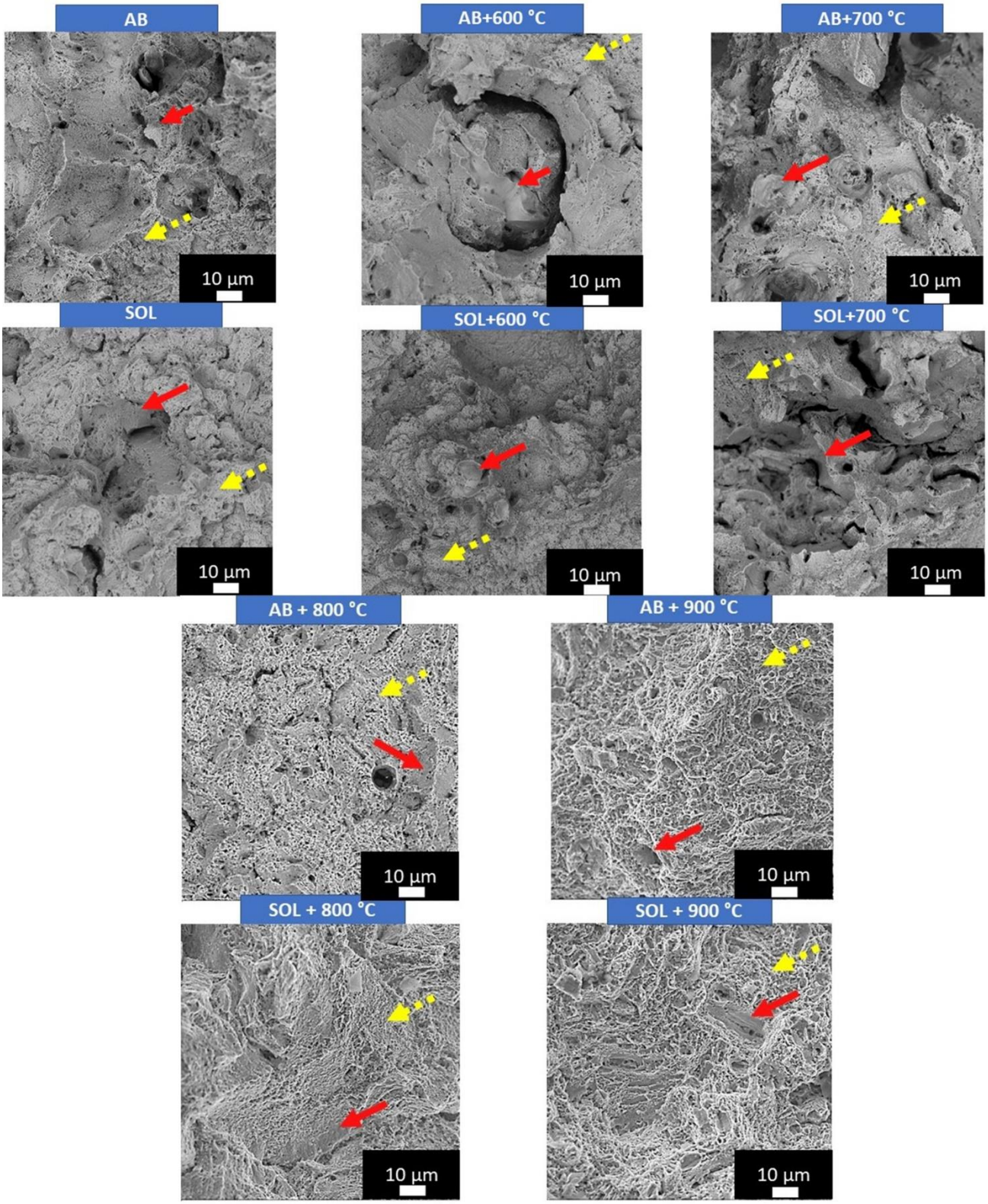

Figure 11 - SEM images of the fracture surfaces of AB, SOL, and different prolonged heat-treated states. Dimples indicated by yellow dash arrows while the brittle fractures are pointed out by red arrows.

The fine dimples of the fracture surfaces are better highlighted in SEM images provided in Figure 12. For the SOL+800 °C and SOL+900 °C states, there are more areas without dimples due to the presence of larger δ phases involving more extensive brittle fractures compared to the AB +800 °C and AB+900 °C conditions.

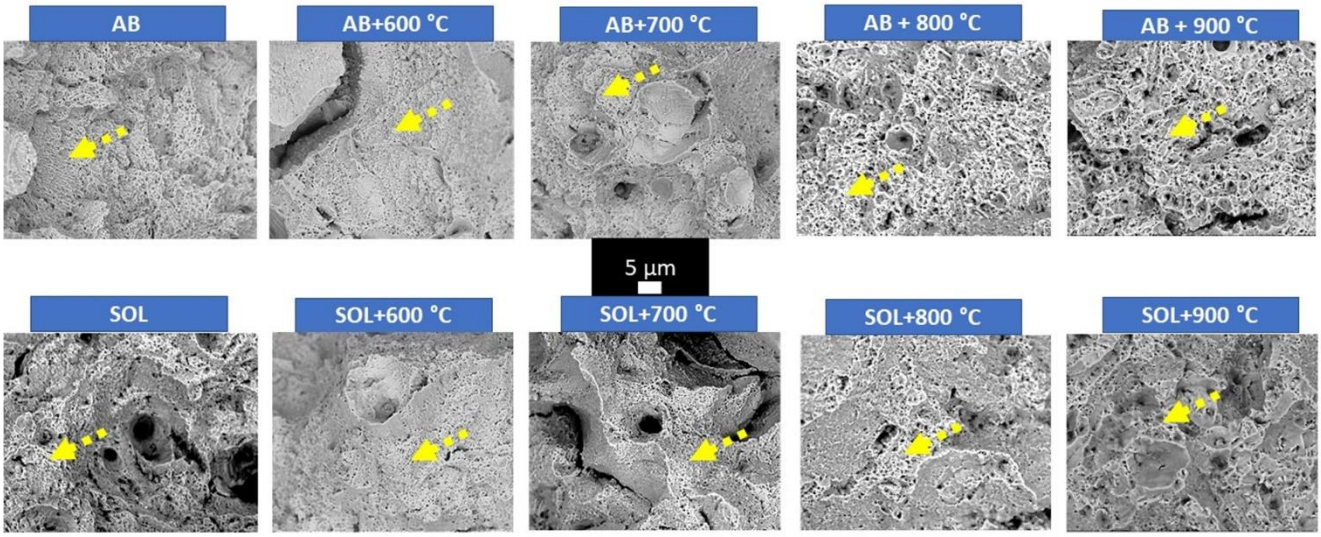

Figure 12 - SEM images revealing areas with dimples (indicated by yellow dash arrows) associated with ductility fractures of the AB, SOL, and different prolonged heat-treated states.

4.0 Conclusions

The microstructure and mechanical stability of AB and SOL states under prolonged thermal exposures from 600 °C to 900 °C for 200 hours were investigated. Thermal exposures at 600 °C promoted the formation of γ" phases. Additionally, 700 °C resulted in the formation of mixed γ" and δ phases, while higher temperature (800 °C and 900 °C) generated the predominant formation of δ phases. The thermally exposed AB states revealed larger numbers but smaller size of δ phases if compared to the prolonged thermal exposure SOL states. This can be ascribed to the inhomogeneous chemical composition of the AB state, which presented areas depleted of Nb, thus limiting the growth of phases.

The tensile properties revealed different evolution for the AB and SOL conditions under thermal exposures for 200 hours. For the AB conditions, the tensile strength and ductility degradations resulted to be similar under thermal exposures from 600 °C to 800 °C. This derives from the reduced growth of the phases induced by the presence of segregations. Differently, the AB+900 °C state revealed the dissolution of dendritic structures resulting in more marked mechanical properties variations. On the other hand, the SOL state presented a homogenous chemical distribution, which exhibited more

significant mechanical properties variations under all the prolonged thermal exposures. In fact, the abundance of Nb homogenous distributed within the alloy allowed the growth of the phases under thermal exposures.

The current work highlights how a different level of chemical homogenization can impact the generation and growth of the phases as well as the mechanical properties.

Data availability

The authors declare that the main data supporting the findings of this work are available within the article.

Declaration of competing interest

The authors declare that they have no known competing financial interests or personal relationships that could have appeared to influence the work reported in this paper.

CRediT author statement

Giulio Marchese: Conceptualization, Methodology, Investigation, Data curation, Writing - original draft and Writing- Reviewing. **Emilio Bassini:** Data curation and Investigation. **Simone Parizia:** Data curation. **Diego Manfredi:** Supervision and Writing- Reviewing. **Daniele Ugues:** Supervision and Writing- Reviewing. **Mariangela Lombardi:** Supervision and Writing- Reviewing. **Paolo Fino:** Supervisor. **Sara Biamino:** Supervision and Writing- Reviewing.

References

[1] D.D. Gu, W. Meiners, K. Wissenbach, R. Poprawe, Laser additive manufacturing of metallic components: materials, processes and mechanisms, Int. Mater. Rev. 57 (2012) 133–164. doi:10.1179/1743280411Y.0000000014.

[2] R. Acharya, J.A. Sharon, A. Staroselsky, Prediction of microstructure in laser powder bed fusion process, Acta Mater. 124 (2017) 360–371. doi:10.1016/j.actamat.2016.11.018.

[3] D. Zhang, W. Niu, X. Cao, Z. Liu, Effect of standard heat treatment on the microstructure and mechanical properties of selective laser melting manufactured Inconel 718 superalloy, Mater. Sci. Eng. A. 644 (2015) 32–40. doi:10.1016/j.msea.2015.06.021.

[4] W.E. Frazier, Metal additive manufacturing: A review, J. Mater. Eng. Perform. 23 (2014) 1917–1928. doi:10.1007/s11665-014-0958-z.

[5] I.A. Choudhury, M.A. El-Baradie, Machinability of nickel-base super alloys: a general review, J. Mater. Process. Technol. 77 (1998) 278–284. doi:10.1016/S0924-0136(97)00429-9.

[6] E.O. Ezugwu, Key improvements in the machining of difficult-to-cut aerospace superalloys, Int. J. Mach. Tools Manuf. 45 (2005) 1353–1367. doi:10.1016/j.ijmachtools.2005.02.003.

[7] Z. Wang, K. Guan, M. Gao, X. Li, X. Chen, X. Zeng, The microstructure and mechanical properties of deposited-IN718 by selective laser melting, J. Alloys Compd. 513 (2012) 518–523. doi:10.1016/j.jallcom.2011.10.107.

[8] G. Marchese, E. Bassini, M. Calandri, E.P. Ambrosio, F. Calignano, M. Lorusso, D. Manfredi, M. Pavese, S. Biamino, P. Fino, Microstructural investigation of as-fabricated and heat-treated Inconel 625 and Inconel 718 fabricated by direct metal laser sintering : contribution of Politecnico di Torino and Istituto Italiano di Tecnologia (IIT) di Torino, Met. Powder Rep. 71 (2016) 273–278. doi:10.1016/j.mprp.2016.06.002.

[9] M.M. Attallah, R. Jennings, X. Wang, L.N. Carter, Additive manufacturing of Ni-based superalloys: The outstanding issues, MRS Bull. 41 (2016) 758–764. doi:10.1557/mrs.2016.211.

[10] L.N. Carter, X. Wang, N. Read, R. Khan, M. Aristizabal, K. Essa, M.M. Attallah, Process optimisation of selective laser melting using energy density model for nickel based superalloys, Mater. Sci. Technol. 32 (2016) 657–661. doi:10.1179/1743284715Y.0000000108.

[11] D. Tomus, P.A. Rometsch, M. Heilmaier, X. Wu, Effect of minor alloying elements on crack-formation characteristics of Hastelloy-X manufactured by selective laser melting, Addit. Manuf. 16 (2017) 65–72. doi:10.1016/j.addma.2017.05.006.

[12] G. Marchese, G. Basile, E. Bassini, A. Aversa, M. Lombardi, D. Ugues, P. Fino, S. Biamino, Study of the microstructure and cracking mechanisms of Hastelloy X produced by laser powder bed fusion, Materials (Basel). 11 (2018). doi:10.3390/ma11010106.

[13] G. Marchese, E. Bassini, A. Aversa, M. Lombardi, D. Ugues, P. Fino, S. Biamino, Microstructural Evolution of Post-Processed Hastelloy X Alloy Fabricated by Laser Powder Bed Fusion, Materials (Basel). 12 (2019). doi:10.3390/ma12030486.

[14] Q. Han, R. Mertens, M.L. Montero-sistiaga, S. Yang, R. Setchi, K. Vanmeensel, B. Van Hooreweder, S.L. Evans, H. Fan, Laser powder bed fusion of Hastelloy X: Effects of hot isostatic pressing and the hot cracking mechanism, Mater. Sci. Eng. A. 732 (2018) 228–239. doi:10.1016/j.msea.2018.07.008.

[15] special Metals, Inconel Alloy 625, (2006). http://www.specialmetals.com/assets/smc/documents/alloys/inconel/inconel-alloy-625.pdf (accessed January 20, 2020).

[16] L.E. Shoemaker, Alloys 625 and 725: Trends in properties and applications, in: E.A. Loria (Ed.), Superalloys 718, 625, 706 Deriv. 2005, TMS (The Minerals, Metals & Materials Society), 2005: pp. 409–418. doi:10.7449/2005/Superalloys_2005_409_418.

[17] G.D. Smith, D.J. Tillack, S.J. Patel, Alloy 625 - Impressive Past/Significant Presence/Awesome Future, in: E.A. Loria (Ed.), Superalloys 718, 625, 706 Var. Deriv., TMS (The Minerals, Metals & Materials Society), 2001: pp. 35–46. doi:10.7449/2001/Superalloys_2001_35_46.

[18] S. Floreen, G.E. Fuchs, W.J. Yang, The Metallurgy of Alloy 625, in: E.A. Loria (Ed.), Superalloys 718, 625, 706 Var. Deriv. Miner. Met. Mater. Socity, TMS (The Minerals, Metals & Materials Society), 1994: pp. 13–37. doi:10.7449/1994/Superalloys_1994_13_37.

[19] M. Kohler, Effect of the elevated-temperature-precpitation in Alloy 625 on properties and microstructure, in: E.A. Loria (Ed.), Superalloys 718, 625, 706 Var. Deriv., TMS (The Minerals, Metals & Materials Society), 1991: pp. 363–374. doi:10.7449/1991/Superalloys_1991_363_374.

[20] J.F. Radavich, A. Fort, Effects of Long Time Exposure in Alloy 625 at 1200°F, 1400°F and 1600°F, in: E.A. Loria (Ed.), Superalloys 718, 625 Var. Deriv., TMS (The Minerals, Metals & Materials Society), 1994: pp. 635–647. doi:10.7449/1994/Superalloys_1994_635_647.

[21] I.J. Moore, J.I. Taylor, M.W. Tracy, M.G. Burke, E.J. Palmiere, Grain coarsening behaviour of solution annealed Alloy 625 between 600–800 °C, Mater. Sci. Eng. A. 682 (2017) 402–409. doi:10.1016/j.msea.2016.11.060.

[22] L.M. Suave, D. Bertheau, J. Cormier, P. Villechaise, A. Soula, Z. Hervier, J. Laigo, Impact of microstructural evolutions during thermal aging of Alloy 625 on its monotonic mechanical properties, in: MATEC Web Conf., 2014. doi:10.1051/matecconf/20141421001.

[23] L.M. Suave, J. Cormier, P. Villechaise, A. Soula, Z. Hervier, D. Bertheau, J. Laigo, Microstructural evolutions during thermal aging of alloy 625: Impact of temperature and forming process, Metall. Mater. Trans. A Phys. Metall. Mater. Sci. 45 (2014) 2963–2982. doi:10.1007/s11661-014-2256-7.

[24] M. Cabrini, S. Lorenzi, C. Testa, F. Brevi, S. Biamino, P. Fino, D. Manfredi, G. Marchese, F. Calignano, T. Pastore, Microstructure and selective corrosion of alloy 625 obtained by means of laser powder bed fusion, Materials (Basel). 12 (2019) 1–11. doi:10.3390/ma12111742.

[25] M. Cabrini, S. Lorenzi, C. Testa, T. Pastore, F. Brevi, S. Biamino, P. Fino, D. Manfredi, G. Marchese, F. Calignano, F. Scenini, Evaluation of Corrosion Resistance of Alloy 625 Obtained by Laser Powder Bed Fusion, J. Electrochem. Soc. 166 (2019) C3399–C3408. doi:10.1149/2.0471911jes.

[26] G. Marchese, M. Lorusso, S. Parizia, E. Bassini, J.-W. Lee, F. Calignano, D. Manfredi, M. Terner, H.-U. Hong, D. Ugues, M. Lombardi, S. Biamino, Influence of heat treatments on microstructure evolution and mechanical properties of Inconel 625 processed by laser powder bed fusion, Mater. Sci. Eng. A. 729 (2018) 64–75. doi:10.1016/j.msea.2018.05.044.

[27] A. Kreitcberg, V. Brailovski, S. Turenne, Elevated temperature mechanical behavior of IN625 alloy processed by laser powder-bed fusion, Mater. Sci. Eng. A. 700 (2017) 540–553. doi:10.1016/j.msea.2017.06.045.

[28] F. Zhang, L.E. Levine, A.J. Allen, M.R. Stoudt, G. Lindwall, E.A. Lass, M.E. Williams, Y. Idell, C.E. Campbell, Effect of heat treatment on the microstructural evolution of a nickel- based superalloy additive-manufactured by laser powder bed fusion, Acta Mater. 152 (2018) 200–214. doi:10.1016/j.actamat.2018.03.017.

[29] E.A. Lass, M.R. Stoudt, M.E. Williams, M.B. Katz, L.E. Levine, T.Q. Phan, T.H. Gnaeupel-Herold, D.S. Ng, Formation of the Ni3Nb δ-Phase in Stress-Relieved Inconel 625 Produced via Laser Powder-Bed Fusion Additive Manufacturing, Metall. Mater. Trans. A Phys. Metall. Mater. Sci. 48 (2017) 5547–5558. doi:10.1007/s11661-017-4304-6.

[30] S. Li, Q. Wei, Y. Shi, Z. Zhu, D. Zhang, Microstructure Characteristics of Inconel 625 Superalloy Manufactured by Selective Laser Melting, J. Mater. Sci. Technol. 31 (2015) 946–952. doi:10.1016/j.jmst.2014.09.020.

[31] M.R. Stoudt, E.A. Lass, D.S. Ng, M.E. Williams, F. Zhang, C.E. Campbell, G. Lindwall, L.E. Levine, The Influence of Annealing Temperature and Time on the Formation of δ-Phase in Additively-Manufactured Inconel 625, Metall. Mater. Trans. A. 49A (2018) 3028–3037. doi:10.1007/s11661-018-4643-y.

[32] G. Lindwall, C.E. Campbell, E.A. Lass, F. Zhang, M.R. Stoudt, A.J. Allen, L.E. Levine, Simulation of TTT Curves for Additively Manufactured Inconel 625, Metall. Mater. Trans. A. 50 (2019) 457–467. doi:10.1007/s11661-018-4959-7.

[33] E.A. Lass, M.R. Stoudt, M.B. Katz, M.E. Williams, Precipitation and dissolution of δ and γ″ during heat treatment of a laser powder-bed fusion produced Ni-based superalloy, Scr. Mater. 154 (2018) 83–86. doi:10.1016/j.scriptamat.2018.05.025.

[34] A. Kreitcberg, V. Brailovski, S. Turenne, Effect of heat treatment and hot isostatic pressing on the microstructure and mechanical properties of Inconel 625 alloy processed by laser powder bed fusion, Mater. Sci. Eng. A. 689 (2017) 1–10. doi:10.1016/j.msea.2017.02.038.

[35] G. Marchese, S. Parizia, M. Rashidi, A. Saboori, D. Manfredi, D. Ugues, M. Lombardi, E. Hryha, S. Biamino, The role of texturing and microstructure evolution on the tensile behavior of heat-treated Inconel 625 produced via laser powder bed fusion, Mater. Sci. Eng. A. 769 (2020) 138500. doi:10.1016/j.msea.2019.138500.

[36] K. Inaekyan, A. Kreitcberg, S. Turenne, V. Brailovski, Microstructure and mechanical properties of laser powder bed-fused IN625 alloy, Mater. Sci. Eng. A. 768 (2019) 138481. doi:10.1016/j.msea.2019.138481.

[37] H. Chandler, ed., Heat Treater' s Guide: Practices and Procedures for Nonferrous Alloys, ASM International, Materials Park, OH, 1996.

[38] M.J. Donachie, S.J. Donachie, Superalloys: A technical Guide, second, ASM International, Materials Park, OH, 2002.

[39] L.M. Suave, D. Bertheau, J. Cormier, P. Villechaise, A. Soula, Z. Hervier, F. Hamon, J. Laigo, Impact of Thermomechanical Aging on Alloy 625 High Temperature Mechanical Properties, 8th Int. Symp. Superalloy 718 Deriv. (2014) 317–331. doi:10.1002/9781119016854.ch26.

[40] V. Shankar, K. Bhanu Sankara Rao, S.. Mannan, Microstructure and mechanical properties of

Inconel 625 superalloy, J. Nucl. Mater. 288 (2001) 222–232. doi:10.1016/S0022-3115(00)00723-6.

[41] J. Mittra, S. Banerjee, R. Tewari, G.K. Dey, Fracture behavior of Alloy 625 with different precipitate microstructures, Mater. Sci. Eng. A. 574 (2013) 86–93. doi:10.1016/j.msea.2013.03.021.